

An Iron Reservoir to the Catalytic Metal

THE RUBREDOXIN IRON IN AN EXTRADIOL DIOXYGENASE*

Received for publication, March 8, 2015, and in revised form, April 10, 2015. Published, JBC Papers in Press, April 27, 2015, DOI 10.1074/jbc.M115.650259

Fange Liu^{‡§1,2}, Jiafeng Geng^{‡¶1,2,3,4}, Ryan H. Gumpfer[‡], Arghya Barman[‡], Ian Davis^{‡¶}, Andrew Ozarowski^{||}, Donald Hamelberg^{‡§¶}, and Aimin Liu^{‡§¶15}

From the [‡]Department of Chemistry, [§]Center for Diagnostics and Therapeutics, and [¶]Molecular Basis of Disease Program, Georgia State University, Atlanta, Georgia 30303 and the ^{||}National High Magnetic Field Laboratory, Florida State University, Tallahassee, Florida 32310

Background: An accessory [Fe(Cys)₄] center of unknown function is present in 3-hydroxyanthranilate 3,4-dioxygenase.

Results: An intermolecular iron shuttling from the [Fe(Cys)₄] site to the catalytic site is observed.

Conclusion: The rubredoxin-like domain is an iron reservoir for the catalytic site when the catalytic metal becomes stripped during metabolic events.

Significance: An iron shuttling mechanism is proposed for the iron-sulfur center.

The rubredoxin motif is present in over 74,000 protein sequences and 2,000 structures, but few have known functions. A secondary, non-catalytic, rubredoxin-like iron site is conserved in 3-hydroxyanthranilate 3,4-dioxygenase (HAO), from single cellular sources but not multicellular sources. Through the population of the two metal binding sites with various metals in bacterial HAO, the structural and functional relationship of the rubredoxin-like site was investigated using kinetic, spectroscopic, crystallographic, and computational approaches. It is shown that the first metal presented preferentially binds to the catalytic site rather than the rubredoxin-like site, which selectively binds iron when the catalytic site is occupied. Furthermore, an iron ion bound to the rubredoxin-like site is readily delivered to an empty catalytic site of metal-free HAO via an intermolecular transfer mechanism. Through the use of metal analysis and catalytic activity measurements, we show that a downstream metabolic intermediate can selectively remove the catalytic iron. As the prokaryotic HAO is often crucial for cell survival, there is a need for ensuring its activity. These results suggest that the rubredoxin-like site is a possible auxiliary iron source to the catalytic center when it is lost during catalysis in a pathway with metabolic intermediates of metal-chelating properties. A spare tire concept is proposed based on this biochemical study, and this concept opens up a potentially new functional paradigm for iron-sulfur centers in iron-dependent enzymes as

transient iron binding and shuttling sites to ensure full metal loading of the catalytic site.

Rubredoxin is a small [Fe(Cys)₄]-containing protein typically involved in electron transfer (ET)⁶ (1), and since its discovery (2), rubredoxin motifs have been increasingly identified in metalloproteins as either primary or accessory metal-binding sites. In fact, over 74,000 non-redundant protein sequences possess a rubredoxin motif,⁷ and a Protein Data Bank survey we conducted revealed more than 2,000 protein structures containing such a mononuclear iron-sulfur center, some contain a bound zinc ion or have an unknown metal identity. Interestingly, some iron-dependent enzymes from single cellular sources, such as superoxide reductase (3) and class III ribonucleotide reductase (4, 5), contain an accessory rubredoxin-like site. The biological functions of the rubredoxin-like site in these enzymes are poorly understood.

3-Hydroxyanthranilate 3,4-dioxygenase (HAO), a non-heme iron(II)-dependent extradiol dioxygenase, catalyzes the oxidative cleavage of the aromatic ring of 3-hydroxyanthranilic acid (3-HAA) by activating molecular oxygen (6). HAO is shared by both the kynurenine pathway in tryptophan metabolism and the prokaryotic 2-nitrobenzoic acid biodegradation pathway (Fig. 1) (7, 8). The first crystal structure determined from *Cupriavidus metallidurans* (9) reveals that this enzyme belongs to the functionally diverse cupin superfamily (10) and that the catalytic iron is anchored by a 2-His-1-carboxylate facial triad ligand set, (His)₂Glu (11). The crystal structures of HAO from

* This work was supported, in whole or in part, by National Institutes of Health Grant GM107529 (to A. L.) and National Science Foundation Grants CHE-1309942 (to A. L.) and MCB-0953061 (to D. H.).

The atomic coordinates and structure factors (codes 4HSJ, 4HVO, 4HVQ, and 4L2N) have been deposited in the Protein Data Bank (<http://www.pdb.org/>).

¹ Both authors contributed equally to this work.

² Supported by a Ambrose H. Pendergrast Graduate Research Fellowship. Present address: Dept. of Chemistry, University of Chicago, Chicago, IL. E-mail: Fangel@uchicago.edu.

³ Present address: School of Chemistry and Biochemistry, GA Institute of Technology, Atlanta, GA. E-mail: jgeng31@mail.gatech.edu.

⁴ Supported by fellowships from the Molecular Basis of Disease Program.

⁵ To whom correspondence should be addressed: Georgia State University, 50 Decatur St. SE, Atlanta, GA 30303. Tel.: 404-413-5532; Fax: 404-413-5505; E-mail: Feradical@gsu.edu.

⁶ The abbreviations used are: ET, electron transfer; ACMS, α -amino- β -carboxymuconate- ϵ -semialdehyde; ACMSD, ACMS decarboxylase; 3-HAA, 3-hydroxyanthranilate; HAO, 3-hydroxyanthranilate 3,4-dioxygenase; PIC, picolinic acid; ICP-OES, inductively coupled plasma optical emission spectroscopy; PDB, Protein Data Bank; "Cu", copper did not bind to the rubredoxin site.

⁷ A secondary sequence search based on the canonical rubredoxin domain (C-X-X-C-G-X(n)-C-P-X-C-G, X(n) is a variable linker) was performed using the motif search feature of www.genome.jp, a service of the Kyoto University Bioinformatics Center. The motif search gave 74,071 non-redundant amino acid sequences from GenBank, UniProt, RefSeq, and PDBSTR.

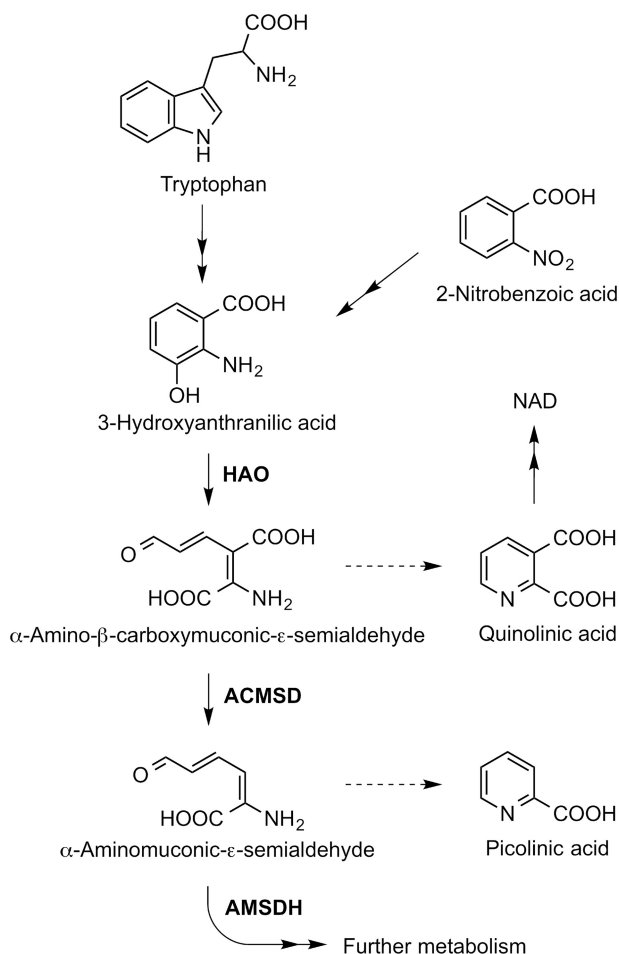


FIGURE 1. HAO catalyzes the oxidative phenyl ring cleavage reaction in the kynurenine pathway that is found in both 2-nitrobenzoic acid biodegradation pathway and L-tryptophan catabolism. HAO employs a mononuclear ferrous iron to activate O_2 . Both oxygen atoms are inserted into the organic substrate.

eukaryotic origins are now available from *Saccharomyces cerevisiae* (12), bovine kidney (13), and human (PDB entry 2QNK).⁸ An unexpected finding is that prokaryotic HAO structures contain two distinct iron-binding domains that are separated by 24 Å in *C. metallidurans* HAO (9), whereas the majority of eukaryotic HAO structures only contain the (His)₂Glu catalytic iron site (Fig. 2). The additional metal site in single-celled organisms is a rubredoxin-like iron center coordinated by four cysteine residues on the protein surface at the C terminus.

Although not involved in catalysis, mutation of the cysteine residues at the rubredoxin-like site caused HAO to be expressed in inclusion bodies (9), indicating a structural role in protein folding. In a previous study (15), the [Fe(Cys)₄] center was shown to be capable of absorbing leaking oxidative equivalents, which prevents protein damage resulting from autoxidation of the ferrous ion at the catalytic site. Although this is an interesting finding, it naturally raises a question: despite the high sequence similarity and structural resemblance to the prokaryotic analogs, why do the vast majority of eukaryotic HAOs

not possess a similar iron center for the same purpose? In the present work, we investigate the rubredoxin-like center of HAO by using analytical (metal analysis), biochemical, spectroscopic, structural, and computational approaches. Our work suggests a new biological function of the rubredoxin center in transient iron binding and shuttling, thereby expanding the functional diversity of this common metal-binding motif.

Experimental Procedures

Chemicals—⁵⁷Fe (95% enrichment) was purchased from Science Engineering and Education Co. (Edina, MN). 3-HAA, ammonium ferrous sulfate hexahydrate, ascorbate, EDTA, copper sulfate pentahydrate, Tris base, and glycerol were purchased from Sigma with the highest grade available.

Bioinformatics Analysis—The evolutionary history of HAO was inferred by using the Maximum Likelihood method based on the JTT matrix-based model (16). The tree with the highest log likelihood (-26530.3730) is shown. Initial tree(s) for the heuristic search were obtained by applying the Neighbor Joining method to a matrix of pairwise distances estimated using a JTT model. The tree is drawn to scale, with branch lengths measured in the number of substitutions per site. All positions with less than 95% site coverage were eliminated. That is, fewer than 5% alignment gaps, missing data, and ambiguous bases were allowed at any position. There was a total of 55 posts in the final dataset. Evolutionary analyses were conducted in MEGA6 (17). Subsequently, a HAO sequence similarity network was constructed with the EFI-EST webserver and visualized with Cytoscape 3.2.0.

Protein Preparation—HAO was purified according to a published method (15). All catalytic activity assays and spectroscopic measurements were performed in 50 mM Tris-HCl, pH 7.6, buffer with 5% glycerol. The metal-free, apo form of HAO was prepared by overnight treatment with EDTA (10 mM) at 4 °C, followed by dialysis and gel-filtration chromatography for removal of EDTA. The fully iron-loaded HAO (holo-HAO) was obtained by adding 10 eq of Fe²⁺ (from a fresh O₂-free solution of ammonium ferrous sulfate) to apo-HAO under anaerobic conditions. Excess iron ions were removed by gel-filtration chromatography using argon-saturated buffer.

Catalytic Activity Assays of Metal-reconstituted HAO—The catalytic activity assays were performed in 50 mM Tris-HCl buffer (pH 7.6, 5% glycerol) as previously described using an Agilent 8453 spectrophotometer (9, 15, 19–21). The rate of enzymatic reactions was monitored based on the formation of the dioxygenation product (Fig. 1), α-amino-β-carboxymuconate-ε-semialdehyde (ACMS), at 360 nm ($\epsilon_{360\text{ nm}} = 47,500\text{ M}^{-1}\text{ cm}^{-1}$) (15). The apoenzyme was premixed and incubated with varying molar equivalents and orders of metals according to Fig. 3. The final concentrations of enzyme and substrate were kept constant throughout all assays. Holo-HAO with 2 molar eq of Fe²⁺ was set as the 100% benchmark for comparison.

Mössbauer Spectroscopy—In an anaerobic chamber, we reconstituted apo-HAO with 1 eq of ⁵⁷Fe²⁺ and/or Cu²⁺ at a time. This procedure generated a series of samples containing ⁵⁷Fe/⁵⁷Fe, ⁵⁷Fe/⁶⁴Cu (copper did not bind to the rubredoxin site), and Cu/⁵⁷Fe. The final protein concentration for Mössbauer measurement was 0.9 mM. Mössbauer spectra were

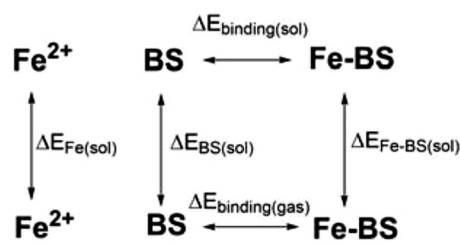
⁸ E. Bitto, C. A. Bingman, G. E. Wesenberg, and G. N. Phillips Jr., 10.2210/pdb2qnk/pdb.

recorded on a constant acceleration instrument at 77 K using a model MS4 instrument manufactured by See Co., Edina, MN.

Electronic Paramagnetic Resonance (EPR) Spectroscopy—The Cu^{2+} -loaded HAO for EPR analysis was generated by reconstitution of apo-HAO with 9 eq of Cu^{2+} (from a fresh solution of copper sulfate pentahydrate), followed by gel-filtration chromatography for removal of excess Cu^{2+} . X-band EPR data were obtained in perpendicular mode (9.62 GHz) on a Bruker ER 200D spectrometer coupled with a 4116DM resonator at 100-kHz modulation frequency under nonsaturating conditions with modulation amplitude of 0.3 millitesla. The measurement temperature was maintained at 77 K using a cold finger liquid nitrogen Dewar. The EPR spectrum was simulated using a program written by one of the authors (22) with the following parameters: $g_x = 2.055$, $g_y = 2.065$, $g_z = 2.256$, $I = 3/2$ for the copper nuclear spin, $I = 1$ for the nitrogen nuclear spin, $A_z(\text{Cu}) = 175$ G, and $A(\text{N}) = 13.4$ G. Two nitrogen atoms from the two histidine ligands were used to reproduce the hyperfine coupling interactions.

Crystallization, X-ray Data Collection, and Data Processing—HAO proteins were crystallized by optimization of conditions previously established (9), using hanging drop vapor diffusion in VDX plates from Hampton Research (Aliso Viejo, CA). Crystal growth was carried out at 16 °C in a vibration-free crystal growth refrigerator (Molecular Dimensions Ltd., Altamonte Springs, FL). Single crystals suitable for x-ray data collection were obtained from drops assembled with 1 μl of protein solution and 1 μl of reservoir solution containing 0.1 M Tris-HCl, pH 9.0, 0.2 M MgCl_2 , 1 mM DTT, and 20% PEG 8000. For the picolinic acid (PIC)-bound HAO structure, the ligand-free crystals were soaked in the mother liquor supplemented with 1 mM PIC. The crystals were mounted in small loops made of fine rayon fiber and flash-frozen in liquid nitrogen after being dipped into the cryoprotectant solution (0.1 M Tris-HCl, pH 9.0, 0.2 M MgCl_2 , 20% PEG 8000, and 30% glycerol). X-ray diffraction data for Fe/Fe-HAO, Fe/"Cu"-HAO, and Cu/Fe-HAO were collected with the SER-CAT beamline 22-ID of the Advanced Photon Source at the Argonne National Laboratory, Argonne, IL. The data collection was performed at 100 K. The diffraction data were indexed, integrated, and scaled with HKL-2000. The structures were solved by molecular replacement using the MOLREP program of the CCP4 suite (23) with the published HAO structure (PDB entry 1YFU) as a search model. Electron density was fit and refined using Coot (24) and REFMAC5 (25).

Molecular Dynamics Simulation—All of the molecular dynamics simulations of Fe/Fe-HAO and single load Fe-HAO with the iron ion bound only to the catalytic site, were performed with the modified version of the ff99SB force field (26) using the AMBER10 suite of programs (27). The 1.74-Å resolution crystal structure of HAO, PDB entry 4L2N from this work, was used as the starting conformation for both systems. The single-loaded Fe-HAO model was generated from the x-ray crystal structure of Fe/Fe-HAO by simply removing one of the irons. The systems were solvated in a periodic rectangular box of the TIP3P water model (28) using the xleap module in the AMBER tools. All of the bonds involving hetero atoms and hydrogen were constrained using the SHAKE algorithm (29).



SCHEME 1

The systems were equilibrated and maintained at 300 K using a Langevin thermostat (30) with a collision frequency of 1 ps^{-1} . Long-range electrostatic interactions were calculated using the Particle mesh Ewald summation method (31), and a cut-off of 9 Å was used for non-bonded interactions. The simulations were performed using the NPT ensemble at a constant pressure of 1 bar, and a time step of 2 fs was used to integrate the equation of motion. The systems were equilibrated for 1 ns, and the final production phases were run for 100 ns. To maintain the crystallographic coordination geometry, harmonic restraints of 300.0 kcal/mol Å² and 60.0 kcal/mol rad² were applied to the coordinating bonds and dihedral angles of the participating residues, respectively, throughout the simulation.

Calculation of Metal-binding Energies—The binding energies of the Fe^{2+} ion at the catalytic site and rubredoxin-like site were calculated based on the thermodynamic cycle shown. From Scheme 1, the following equation can be obtained,

$$\Delta E_{\text{binding(sol)}} = \Delta E_{\text{binding(gas)}} + \Delta E_{\text{Fe-BS(sol)}} - (\Delta E_{\text{BS(sol)}} + \Delta E_{\text{Fe(sol)}}) \quad (\text{Eq. 1})$$

where BS corresponds to the iron binding site. The active site consists of His-51, His-95, Glu-57, and the two water molecules, with and without iron. The rubredoxin-like site consists of Cys-125, Cys-128, Cys-162, and Cys-165, with and without the iron. Ten snapshots from each simulation (Fe/Fe-HAO and single load Fe-HAO) were taken from the last 50 ns of the entire simulation. Each binding site was subjected to single point calculations using the B3LYP/6-31G(d) level of theory. Implicit dielectric of 78.35 was used for the solvent calculations. The $\text{p}K_a$ values of the coordinating residues in the catalytic site and the (Cys)₄ site were estimated using the snapshots from the simulation trajectories. H++ (32) was used to calculate the $\text{p}K_a$ value of the residues. The average $\text{p}K_a$ values of Cys-125, Cys-128, Cys-162, and Cys-165 of the (Cys)₄ site were estimated to be 11.1 ± 0.5 , 10.9 ± 0.3 , 11.1 ± 0.4 , and 10.9 ± 0.3 , respectively, above the intrinsic Cys $\text{p}K_a$ of ~ 8.3 . The average $\text{p}K_a$ values for His-51 and His-95 in the catalytic site were calculated to be 11.4 ± 0.3 and 8.2 ± 0.4 , respectively, also above the intrinsic His $\text{p}K_a$ of ~ 6 . These results suggest that these residues are protonated before iron binding. As the protonation state of these residues changes upon Fe^{2+} binding, an additional term E_p was added to the calculation to account for the dissociation of protons. The deprotonation energy was derived from the calculated $\text{p}K_a$ values as $\Delta G = 2.303 \times RT \times \text{p}K_a$ for each residue, and E_p is the sum of all the ΔG . $\Delta E_{\text{Fe(sol)}}$ is the same for both sites. Therefore, it does not contribute to the estimated binding energy difference between the two locations.

A Spare Tire to the Catalytic Metal

$$\Delta E_{\text{binding(sol)}} = \Delta E_{\text{binding(gas)}} + \Delta E_{\text{Fe-BS(sol)}} - (\Delta E_{\text{BS(sol)}} + \Delta E_{\text{Fe(sol)}}) + E_p \quad (\text{Eq. 2})$$

Catalytic Activity Assays of Apo-HAO to Cu/Fe-HAO or Holo-HAO Pseudo-titrations—Cu/Fe-HAO or holo-HAO was premixed with apo-HAO at different ratios ranging up to 8 eq. The catalytic activity of each sample was measured at a saturating substrate concentration of 200 μM 3-HAA with the final concentration of Cu/Fe-HAO or holo-HAO at 10 nM. For each sample, the residual activity from apo-HAO was deducted from the observed activity to determine the effective activity for comparison. The data were fitted to the Hill equation.

Quantification of Metal Chelation by Metabolic Intermediates—For the experiments performed on apoprotein, HAO (50 μM) was reconstituted with 1 eq of Fe^{2+} , followed by gel filtration chromatography to remove the unbound metal. The single-loaded Fe-HAO was incubated overnight, while stirring with 2 mM 3-HAA or PIC anaerobically on ice in the presence of 2 mM sodium ascorbate to avoid autoxidation. The protein samples were then buffer-exchanged via gel filtration chromatography to remove the 3-HAA and PIC. Steady-state kinetic assays and inductively coupled plasma optical emission spectroscopy (ICP-OES) were performed to quantify the activity and metal content for each sample. The steady-state kinetic assays were performed using a similar protocol as mentioned above and in the presence of 200 μM 3-HAA. The ICP-OES metal analyses were performed using a Varian 720-ES spectrometer. The protein-bound iron was detected at 238.204 nm. A calibration curve was constructed for iron quantification. Yttrium (371.029 nm) was used as an internal standard. For the *ex vivo* experiments performed on the *Escherichia coli* cell lysates containing overexpressed HAO, the cell culture was grown, induced, harvested, and lysed using the same protocol as reported previously (15). The cell lysates were incubated with 2 mM 3-HAA or PIC on ice overnight while stirring, and the target protein HAO was purified using a nickel affinity column and desalted. The subsequent kinetic and spectroscopic analyses were performed using the same procedures as the previous experiments. For each set of experiments, *p* values were calculated to determine the statistical difference between the control sample and the experimental samples.

Results

Bioinformatics Analysis of HAO Shows the Conservation of the Rubredoxin-like Motif—To better understand the evolutionary origins of the $[\text{Fe}(\text{Cys}_4)]$ site, a phylogenetic study was conducted. A blast search for HAO-like proteins returned 1396 results, among which 966 sequences correspond to HAO. Of the HAO proteins returned, 207 partial or redundant sequences were removed, leaving 759 for phylogenetic analysis. Multiple sequence alignment gave two distinct groups of HAO enzymes. The first group (576 sequences) is comprised of bacterial and fungal sources with roughly 170 amino acids in length, and all but four contain a rubredoxin-like motif. The second group (259 sequences) is comprised mostly of animal sources and some fungi sources with an average length of more than 280 amino acids. This group does not contain the canonical rubre-

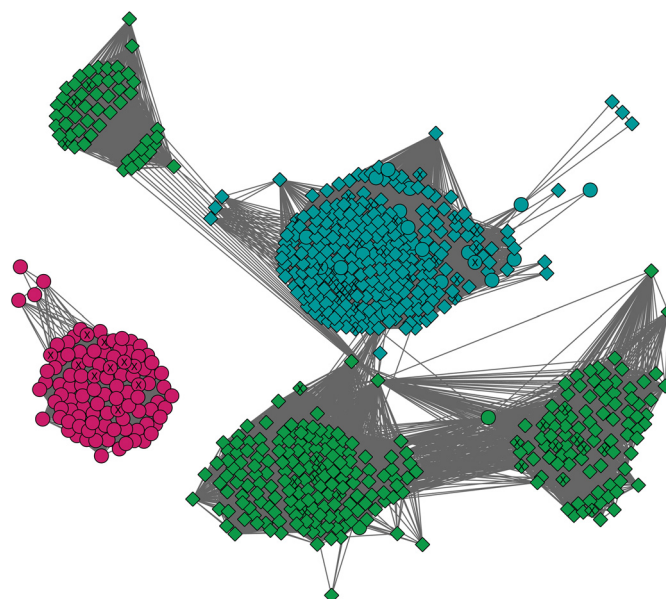


FIGURE 2. HAO sequence similarity network showing the conservatively of the rubredoxin-like domain. A total number of 705 non-redundant HAO sequences were included in the network. Sequences that contain a rubredoxin-like site are *diamonds* and those without are *circles*. The connections less than *E* value of 50 are shown in *gray lines*. Bacteria are shown in *green*, fungi in *teal*, animals in *red*, and *circles* marked with an *X* represent the HAOs that have been previously studied at the protein level.

doxin-like motif, with the exception of *Tupaia chinesis*, a tree shrew. By using the EFI-EST webserver, we also analyzed HAO sequences from the InterPro family IPR010329 and the Pfam family PF06052 and built a HAO sequence similarity network (Fig. 2). The finding, that most prokaryotic organisms utilize the secondary iron-binding site, whereas eukaryotic organisms do not, sparked the initial investigation into the functional role of this accessory metal-binding site.

The Catalytic Center Has a Higher Priority for Metal Binding—The first biochemical issue to be addressed in this study is to compare the metal-binding affinity between the two iron centers. We began by comparing the relative activity of HAO loaded with varying amounts of different transition metals. Using holo-HAO as the catalytic activity benchmark (specific activity 8.6 $\mu\text{mol min}^{-1} \text{mg}^{-1}$) (15), we tested the catalytic activity of apo-HAO reconstituted with Fe^{2+} and Cu^{2+} in different sequences and ratios (Fig. 3). Copper is chosen because it can be characterized by EPR spectroscopy, and its EPR signal is sensitive to the coordination environment. In contrast, zinc ion denatures HAO in the reconstitution experiments, and it is spectroscopically silent. When 2 eq of Cu^{2+} were titrated to apo-HAO, only nominal activity (about 2%) was detected, similar to the apoprotein. This indicates that the Cu^{2+} ion cannot effectively mediate the catalytic ET from 3-HAA to molecular oxygen. When apo-HAO was reconstituted with 1 molar eq of Fe^{2+} per polypeptide chain, the resulting single-loaded Fe-HAO exhibited greater than 80% relative activity, which suggests that Fe^{2+} preferentially binds to the catalytic site. Unlike the α -ketoglutarate-dependent dioxygenase assays in which uncoupled reaction often takes place due to the presence of the co-substrate, α -ketoglutarate (33, 34), the HAO reaction only involves the oxidation of one organic substrate, 3-HAA. Both

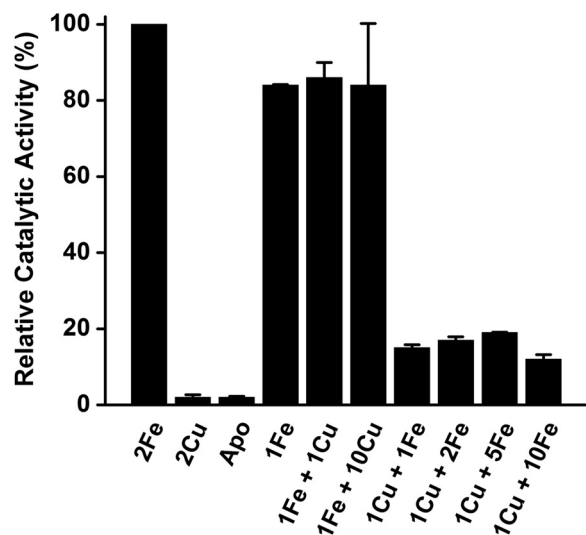


FIGURE 3. **Specific activity of metal-reconstituted HAO.** The first available metal appears to bind to the catalytic center. Apo-HAO was reconstituted with different molar equivalents and orders of metal ions as specified in each column. The catalytic activity of holo-HAO reconstituted with 2 molar eq of Fe^{2+} per protomer (specific activity $8.6 \mu\text{mol min}^{-1} \text{mg}^{-1}$) was assigned at 100% for comparison.

holo-HAO and single-loaded Fe-HAO were robust catalysts under turnover conditions and the differential in self-inactivation was not observed. This suggests that the previously speculated role of protection against autoxidation is insignificant during catalysis, and oxygen activation in HAO is primarily triggered by its sole organic substrate, 3-HAA.

The addition of Cu^{2+} , from 1 to 10 eq, to the single-loaded Fe-HAO caused no appreciable change in its catalytic activity, suggesting that Cu^{2+} is unable to outcompete Fe^{2+} from the catalytic site. Similarly, no apparent increase in the catalytic activity was observed after further addition of Fe^{2+} to single-loaded Cu-HAO, which indicates that Cu^{2+} is able to bind to the catalytic site and is not easily displaced by Fe^{2+} . These results imply that the catalytic site appears to have a higher metal-binding affinity than the surface rubredoxin-like site.

To further quantify the results of the kinetic tests, the order of metal binding was further studied using Mössbauer spectroscopy. In this study, a combination of the Mössbauer-active metal, iron, and a Mössbauer-silent metal, copper, were used and the sequence of metal reconstitution was varied to elucidate the metal binding priority between the two sites in HAO. Under anaerobic conditions, apo-HAO was reconstituted with $^{57}\text{Fe}^{2+}$ and/or Cu^{2+} , 1 eq at a time. This procedure generated a series of samples, which presumably contained $^{57}\text{Fe}/^{57}\text{Fe}$, $^{57}\text{Fe}/\text{Cu}$, and $\text{Cu}/^{57}\text{Fe}$ reconstituted in the specified orders. The Mössbauer spectrum of the $^{57}\text{Fe}/^{57}\text{Fe}$ -HAO sample consists of two distinct sets of quadrupole doublets with roughly equal signal intensities (Fig. 4A, top panel). Spectral simulation shows that the quadrupole doublet represented in red displays an isomer shift (δ) value of 1.37 mm/s and a quadrupole splitting (ΔE_Q) value of 2.95 mm/s. These values are consistent with nitrogen/oxygen mixed ligation for a high-spin ($S = 2$) Fe^{2+} center and are comparable with the values reported for the catalytic Fe^{2+} center in another extradiol dioxygenase, proto-catechuate 4,5-dioxygenase (35). This quadrupole doublet is

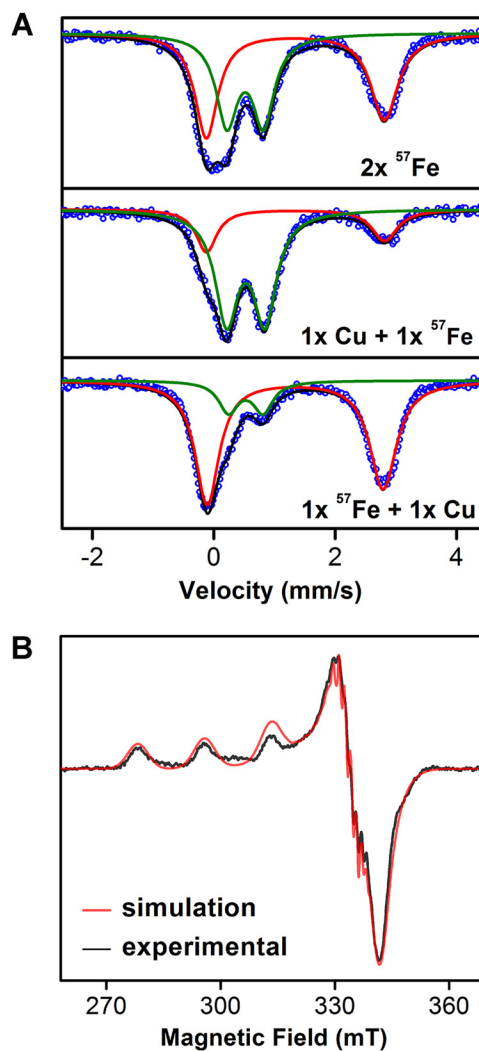


FIGURE 4. **Spectroscopic characterization reveals the metal identity of metal-reconstituted HAO.** A, Mössbauer spectra of HAO reconstituted with 2 eq of $^{57}\text{Fe}^{2+}$ (top panel), 1 eq of Cu^{2+} + 1 eq of $^{57}\text{Fe}^{2+}$ (middle panel), and 1 eq of $^{57}\text{Fe}^{2+}$ + 1 eq of Cu^{2+} (bottom panel). The black line overlaid on the experimental data (blue circles) is the composite simulation. Each of the spectra contains two sets of quadrupole doublets as shown in red and green. The Mössbauer parameters of the two sets of doublets are described in the text. B, X-band EPR spectrum of Cu^{2+} -reconstituted HAO with resolved hyperfine structures obtained at 77 K along with overlaid spectral simulation.

therefore assigned to the iron ion at the catalytic center. The other quadrupole doublet represented in green has a δ value of 0.52 mm/s and a ΔE_Q value of 0.57 mm/s, characteristic of a ferrous rubredoxin-like center at an $S = 2$ state (36, 37). The Mössbauer spectrum of $\text{Cu}/^{57}\text{Fe}$ -HAO was dominated by the signal from the rubredoxin-like center, whereas the catalytic center only accounted for a minimal portion (Fig. 4A, middle panel). Conversely, when $^{57}\text{Fe}^{2+}$ was loaded before Cu^{2+} ($^{57}\text{Fe}/\text{Cu}$ -HAO), the majority of the signal was seen from the catalytic center (Fig. 4A, bottom panel). The Mössbauer data provides a strong support for the notion that the catalytic center has a higher priority for metal binding.

The reconstituted HAO proteins were also analyzed by EPR spectroscopy. The Cu^{2+} center is EPR-active, whereas the Fe^{2+} centers are invisible with X-band EPR spectroscopy at 9 GHz. Due to spin coupling between free Cu^{2+} ions in solution, the EPR signal intensity of free Cu^{2+} ions is low. Binding to protein

A Spare Tire to the Catalytic Metal

ligands, however, increases the EPR signal intensity so that it is proportional to the amount of the chelated copper ions. Chelation also alters the EPR signal line shape and hyperfine structures, which are sensitive to the ligand set and protein environment. Cu^{2+} -reconstituted HAO displays a homogeneous EPR signal indicative of a type II Cu^{2+} center coordinated by a mixture of nitrogen/oxygen ligands (Fig. 4B). The hyperfine splitting pattern can be satisfactorily fit by incorporating the coupling interactions from two nitrogen atoms (nuclear spin $I = 1$), suggesting that Cu^{2+} is solely coordinated to the catalytic $(\text{His})_2\text{Glu}$ site, consistent with the activity assays and Mössbauer studies.

To further evaluate the above biochemical and spectroscopic findings, the metal binding energies at both sites were calculated using the density functional theory at the B3LYP/6-31G(d) level of theory on multiple structural snapshots obtained from 100-ns molecular dynamics simulations of Fe/Fe-HAO based on the scheme described under "Experimental Procedures." The calculated binding energy ($\Delta E_{\text{binding}}$) of Fe^{2+} to the catalytic $(\text{His})_2\text{Glu}$ site is -93.50 ± 3.92 kcal/mol, lower than the binding energy of Fe^{2+} to the rubredoxin-like $(\text{Cys})_4$ site (-83.35 ± 2.67 kcal/mol). The absolute binding free energies are expected to be higher than the change in energies, because the loss in translational entropy of iron upon binding is not considered and is the same for both sites. The difference in binding energy between the two iron-binding sites is ~ 10 kcal/mol and will not be affected by the inclusion of the entropy change. This energy difference provides a rationale for the experimental observation that the first available metal ended up in the enzyme active site.

Structural Characterization Clarifies the Molecular Basis of Metal Binding—Spectroscopic characterization and computational studies confirm the prioritized metal binding between the two metal-binding sites. However, they provide very limited metal center coordination information in the reconstituted proteins. Fe/Fe-, Cu/Fe-, and Fe/"Cu"-HAO proteins generated by the same method as the Mössbauer samples were crystallized, and their structures were determined (Fig. 5). The crystallographic data collection and refinement statistics are summarized in Table 1. The Fe/Fe- and Cu/Fe-HAO crystal structures were refined to 1.74 and 1.75 Å, respectively (Fig. 5, A and B), which allows for detailed comparisons (PDB codes 4HSJ, 4HVO, 4HVQ, and 4L2N). The overall structures of Cu/Fe-HAO and Fe/Fe-HAO are nearly identical. In the catalytic center of Cu/Fe-HAO, the metal ion is coordinated by His-51 and His-95 with bond lengths of 1.9 and 2.0 Å, respectively, whereas in Fe/Fe-HAO, the bond distances are 2.2 Å for both residues. Glu-57 bidentately chelates the catalytic metal in both Cu/Fe and Fe/Fe HAO, with O ϵ 1 and O ϵ 2 at 2.6 and 2.0 Å, respectively in the former, and 2.7 and 2.2 Å, respectively, in the latter. Three water ligands, at distances of 2.3, 2.8, and 2.9 Å from the catalytic center, are observed in Cu/Fe-HAO, whereas two are observed in Fe/Fe-HAO at distances of 2.3 and 2.7 Å. Given the coordination difference to the Fe/Fe-HAO structure and the aforementioned activity assays and spectroscopic results, the metal at the catalytic site in Cu/Fe-HAO is assigned to copper. The other metal center in Cu/Fe-HAO is structurally identical to the $[\text{Fe}(\text{Cys})_4]$ center in the Fe/Fe-HAO structure.

In the Fe/"Cu"-HAO structure shown in Fig. 5C, the metal coordination at the catalytic center closely resembles that of Fe/Fe-HAO. Notably, an inspection of the rubredoxin-like region of Fe/"Cu"-HAO reveals that the electron density of residues 154–174 (11.5% of the total sequence) is missing. As indicated by their higher *B*-factor values (Fig. 5D), the Cu/Fe-HAO structure is slightly more dynamic than the Fe/Fe-HAO structure, whereas the Fe/"Cu"-HAO structure shows significantly increased conformational flexibility near the $(\text{Cys})_4$ site, which is presumably due to the absence of the iron ion at this site. The observed disorder at the rubredoxin-like site seems to have a limited effect on the catalytic site. Therefore, the conformational flexibility at the $(\text{Cys})_4$ site is unlikely to cause a severe disruption in catalysis. These results are consistent with the spectroscopic conclusions that the first metal introduced to apo-HAO binds to the catalytic site and they also reveal that the $(\text{Cys})_4$ site is selective for Fe^{2+} rather than Cu^{2+} .

The flexibility of the $(\text{Cys})_4$ site was further investigated using molecular dynamics simulations. We performed two 100-ns simulations of Fe/Fe-HAO and single load Fe-HAO with the $(\text{Cys})_4$ site free of iron. The *B*-factors were calculated using the simulation trajectory of the Fe/Fe-HAO system and compared with the experimental values from our x-ray crystallographic structure (PDB entry 4L2N) (Fig. 6A). The calculated *B*-factors are in excellent agreement with the experimental results, suggesting that the molecular simulations capture the underlying dynamics of the systems. In general, the peaks (flexible regions) in the simulations nicely coincide with those from the x-ray crystallographic data. During the simulation, the root mean square deviation from ideal geometry of Fe/Fe-HAO is consistently lower than that from single load Fe-HAO, suggesting that single load HAO is more dynamic than Fe/Fe-HAO due to the more flexible C terminus from the former (Fig. 6B). The percentage increase in root mean square fluctuation of Cys-162 and Cys-165 of the $(\text{Cys})_4$ site from Fe/Fe-HAO to single load Fe-HAO is ~ 60 and 70%, respectively, also in line with the x-ray crystallographic results that could not resolve residues 154–174 at the C terminus due to increased flexibility (Fig. 6C).

Restoration of the Catalytic Activity of the Apoprotein Is Observed through Intermolecular Iron Transfer—We noticed that the structure of the rubredoxin motif in HAO is highly analogous to that of iron-chaperone proteins such as Dph4, a unique J-protein family member that preferably binds Fe^{2+} at its $(\text{Cys})_4$ site for the regulation of iron homeostasis (38). The $[\text{Fe}(\text{Cys})_4]$ region is composed of two loop structures forming a metal-binding knuckle (Fig. 7). Thus, it is reasonable to speculate that the $(\text{Cys})_4$ center of HAO would serve as an endogenous iron reservoir for replenishing the catalytic iron when it is lost during highly active metabolic state.

To test this hypothesis, a series of pseudo-titration activity assays were designed to probe the possibility of intermolecular iron transfer from the rubredoxin-like site to the empty catalytic site. As described previously, Cu/Fe-HAO has a Cu^{2+} ion bound at the catalytic center and an Fe^{2+} ion bound at the rubredoxin-like site. This reconstituted form of HAO has minimal catalytic activity, as shown in Fig. 3. However, when inactive, apo-HAO was added to Cu/Fe-HAO, a distinct increase in the dioxygenase activity was observed. The experiment was

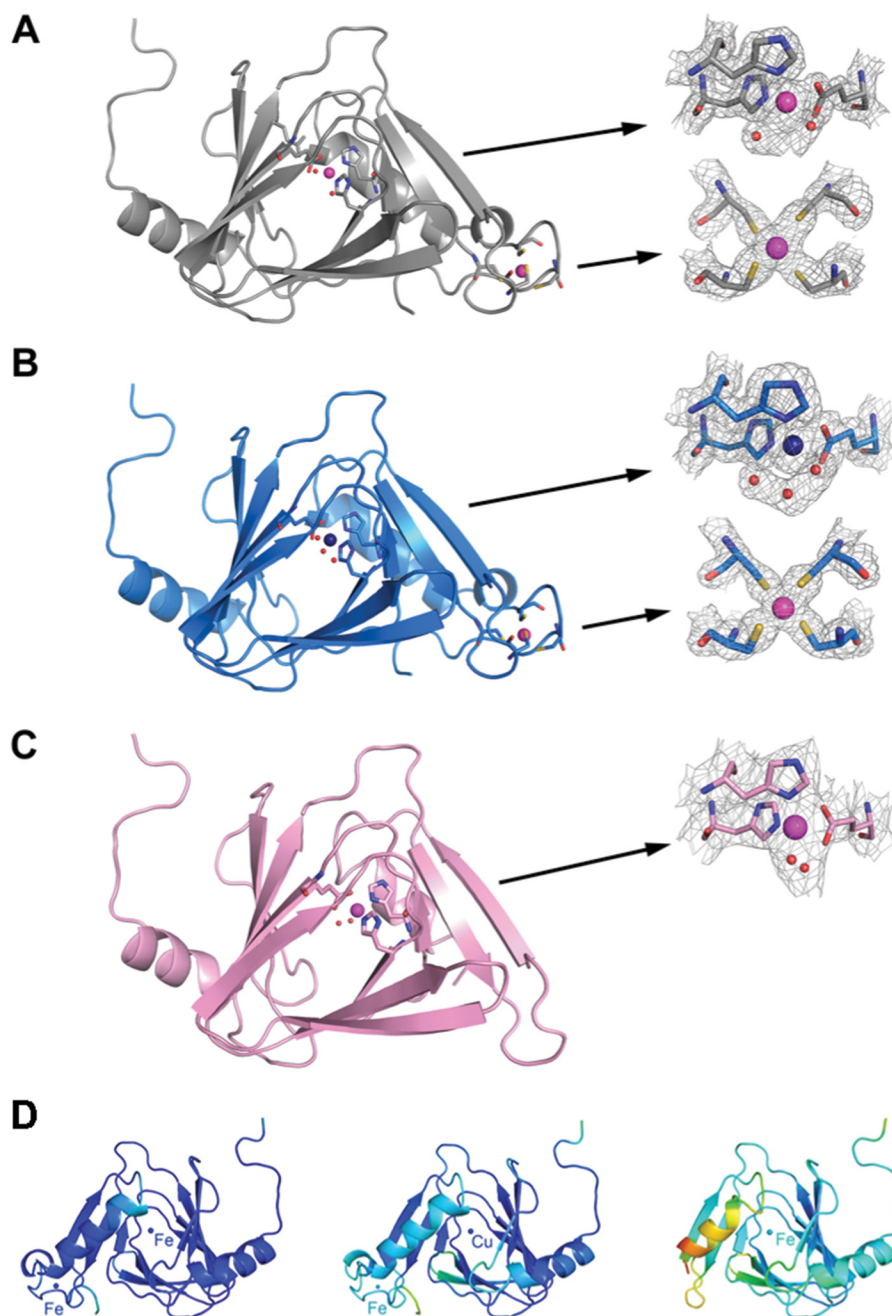


FIGURE 5. X-ray crystallography describes structural details of metal-reconstituted HAO. Ribbon diagrams of (A) Fe/Fe-HAO (gray, 1.74 Å resolution), (B) Cu/Fe-HAO (blue, 1.75 Å resolution), and (C) Fe/Cu-HAO (pink, 2.81 Å resolution) with a zoomed-in view on the catalytic and rubredoxin-like sites. The metal ions are represented by large magenta spheres, whereas water molecules are shown in small red spheres. The rubredoxin-like region (amino acids 154–174) is missing in the Fe/Cu-HAO structure. The $2F_o - F_c$ electron density maps of the two iron-binding sites are also presented and countered to 1.0 σ . D, B-factor value plots show that the structure of the rubredoxin-like site is dynamic in the absence of iron ion. The colors gradually change from dark blue to green and to orange with increasing B-factor values.

performed in a pseudo-titration manner, by premixing Cu/Fe-HAO and apo-HAO at different ratios, with the final concentration of Cu/Fe-HAO kept constant. Fig. 8A shows that the catalytic activity was increasingly restored as the molar ratio of apo-HAO to Cu/Fe-HAO increased. The specific activity increased non-linearly, reaching a plateau corresponding to the catalytic activity of HAO with a single iron ion charged to the catalytic center. Because both forms of protein are minimally active, the mechanism for the rescue of the dioxygenase activity is solely dependent upon intermolecular iron transfer from the

rubredoxin-like site of Cu/Fe-HAO to the catalytic site of apo-HAO.

We then performed a similar set of experiments using holo-HAO rather than Cu/Fe-HAO. Fig. 8B shows that the specific activity increased with increasing apo-HAO concentrations. The specific activity increased non-linearly and reached a plateau at roughly twice the activity of the initial holo-HAO. The result of the experiments with holo-HAO reinforces the mechanistic proposal for an intermolecular iron transfer from the $[\text{Fe}(\text{Cys})_4]$ center to the empty catalytic His₂Glu site.

TABLE 1
X-ray crystallography data collection and refinement statistics of HAO

	Fe/Fe-HAO	Cu/Fe-HAO	Fe/"Cu"-HAO	PIC-bound HAO
Data collection				
Space group	<i>P</i> 6 ₅ 22			
Unit cell lengths (Å)	<i>a</i> = <i>b</i> = 58.3, <i>c</i> = 231.4	<i>a</i> = <i>b</i> = 58.5, <i>c</i> = 230.2	<i>a</i> = <i>b</i> = 57.7, <i>c</i> = 232.0	<i>a</i> = <i>b</i> = 58.59, <i>c</i> = 230.97
Resolution (Å) ^a	50.00-1.74 (1.78-1.74)	45.00-1.75 (1.78-1.75)	45.00-2.80 (2.85-2.80)	50.00-1.88 (1.91-1.88)
Completeness (%) ^a	96.9 (76.8)	98.2 (84.3)	82.9 (22.7)	91.1 (90.3)
<i>R</i> _{merge} (%) ^{a,b}	8.7 (47.4)	11.2 (60.6)	8.8 (35.4)	6.5 (27.5)
<i>I</i> / <i>σ</i> ² ^a	67.2 (3.0)	51.6 (2.5)	30.6 (3.1)	78.9 (6.1)
Redundancy ^a	23.0 (10.0)	25.3 (13.7)	16.1 (10.5)	28.3 (15.4)
Refinement				
Resolution (Å)	1.74	1.75	2.81	1.88
No. reflections; working/test	24,184/1,239	23,111/1,242	4,970/224	19,913/1,018
<i>R</i> _{work} ^c	0.21	0.21	0.22	0.21
<i>R</i> _{free} ^d	0.25	0.24	0.33	0.25
Ramachandran statistics ^e				
Preferred (%)	97.7	97.7	86.2	97.1
Allowed (%)	2.3	2.3	10.5	2.91
Root mean square deviation				
Bond lengths (Å)	0.007	0.027	0.008	0.008
Bond angles (°)	1.17	2.274	1.170	1.170
Database deposition				
PDB entry	4L2N	4HVO	4HVQ	4HSJ

^a Values in parentheses are for the highest resolution shell.

^b $R_{\text{merge}} = \frac{\sum_i |I_{hkl,i} - \langle I_{hkl} \rangle|}{\sum_i I_{hkl,i}}$, where $I_{hkl,i}$ is the observed intensity and $\langle I_{hkl} \rangle$ is the average intensity of multiple measurements.

^c $R_{\text{work}} = \frac{\sum_i |F_o| - |F_c|}{\sum_i |F_o|}$, where $|F_o|$ is the observed structure factor amplitude, and $|F_c|$ is the calculated structure factor amplitude.

^d R_{free} is the *R* factor based on 5% of the data excluded from refinement.

^e Based on values attained from refinement validation options in COOT.

The Need for Replenishing the Catalytic Iron Is Demonstrated by HAO Incubation with a Downstream Metabolic Intermediate—Many of the metabolites in the kynurenine pathway are iron chelators (39–42). In fact, the substrate for HAO, 3-HAA, is excreted in a yeast species and has been suggested to mediate iron metabolism (43, 44) and a downstream metabolic intermediate, PIC (see Fig. 1), is an abundant metal chelator in human milk (39, 40), and it is an inhibitor of HAO (45). During high metabolic activity, these metal-chelating intermediates could potentially outcompete HAO for its non-heme iron ion at the catalytic center. We performed kinetic and spectroscopic studies to investigate the possibility of iron removal by these compounds. HAO reconstituted with 1 eq of Fe²⁺, which preferably binds to the catalytic site, was anaerobically incubated with 3-HAA and PIC. As shown in Fig. 9A, the sample incubated with PIC shows decreased activity compared with the control, whereas there was little change for the sample incubated with 3-HAA. ICP-OES data demonstrates that a single round of incubation with PIC removed nearly half of the iron ions bound to HAO, consistent with the results of the activity assay (Fig. 9B). Furthermore, in an attempt to probe whether this observation would occur in cellular matrix, we performed *ex vivo* experiments using *E. coli* cell lysates that contain over-expressed HAO. Fig. 9, C and D, confirm that PIC can effectively remove iron from HAO and cause a decrease in the catalytic activity.

To follow up on this finding, we were able to determine the PIC-bound crystal structure of HAO to 1.88-Å resolution by soaking ligand-free crystals in mother liquor spiked with PIC (Fig. 10, PDB entry 4HSJ). The binding of PIC did not change the overall structure of HAO (Fig. 10A). The PIC molecule is present only at the catalytic center but not in the [Fe(Cys)₄] center. The PIC ligand bidentately chelates the catalytic iron with the pyridine nitrogen atom (2.4 Å distance) and one of the carboxylate oxygen atoms (2.8 Å), opposite to the metal ligands

His-51, Glu-57, and His-95 (Fig. 10B). In addition, PIC is engaged with Glu-110 via hydrogen-bonding interactions. Fig. 10C shows an overlay of the active site structure of PIC-bound HAO and the previously determined HAO in complex with the substrate 3-HAA (PDB entry 1YFY) (9). There are no significant deviations in the overall structure as well as the metal ligands from the 2-His, 1-Glu facial triad. 3-HAA also bidentately chelates the active site iron at the same position, although its ring structure does not overlay with that of PIC (Fig. 10C). Furthermore, a similar H-bonding interaction with Glu-110 also exists to stabilize 3-HAA. The structural data provides a comprehensive, molecular level of understanding of the HAO-PIC interactions.

Discussion

Consideration of the Roles of the Rubredoxin-like Site—The rubredoxin-like mononuclear iron center is the simplest iron-sulfur center with tetrahedral coordination of the iron ion. The Cys residues form a characteristic loop structure known as a “knuckle” (Cys-X-X-Cys-X-X) (46). A mysterious rubredoxin center is present in HAO. In this work, the following functional roles were considered for the [Fe(Cys)₄] center of HAO in addition to the known oxidative protection aptitude and the default structural role: catalytic, electron transfer, substrate or product channeling, and metal reservoir.

The possibility of the catalytic role does not apply to this enzyme. The accessory, non-heme iron center is clearly not involved in catalysis as shown in our kinetic assays (Fig. 3). All four electrons needed for O₂ reduction are provided by the organic substrate, 3-HAA, thereby eliminating the requirement for electron transfer from an additional electron source. Thus, the most common electron transfer role of the [Fe(Cys)₄] center, *i.e.* electron transfer, is excluded. As to the possibility of substrate or product channeling, the HAO catalytic center has a well defined substrate-binding pocket adjacent to the catalytic

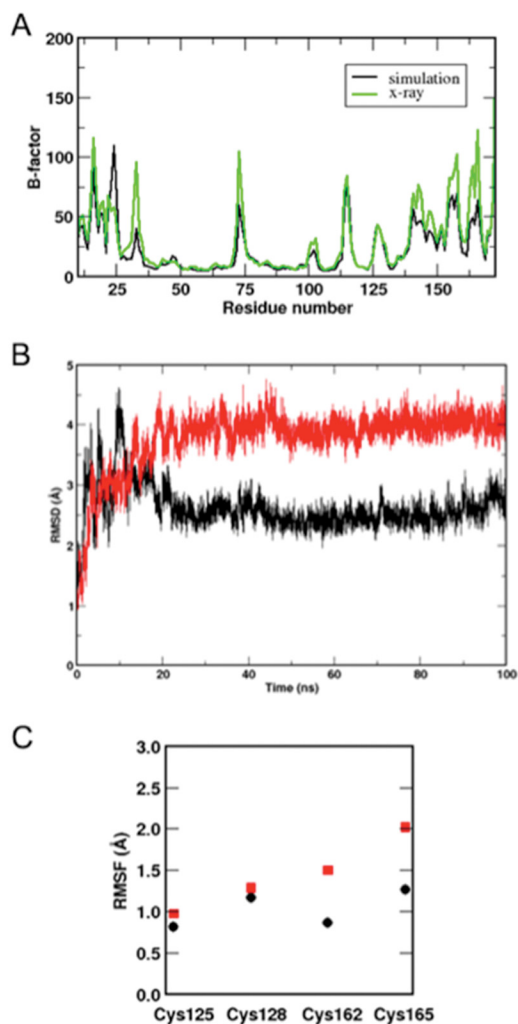


FIGURE 6. **Computational studies of rubredoxin-like site of HAO.** *A*, the comparison of the calculated and experimental *B*-factors of Fe/Fe-HAO. The *B*-factors were calculated from the simulation trajectory of the Fe/Fe-HAO simulation (black) and compared with the *B*-factors from the x-ray crystallographic data (green). *B*, root mean square deviation during molecular dynamics simulations. Root mean square deviation of Fe/Fe-HAO (black) and single load Fe-HAO with the rubredoxin-like site free of metal (red). *C*, root mean square fluctuation of Cys-125, Cys-128, Cys-162, and Cys-165 in Fe/Fe-HAO and single load Fe-HAO. The residues are more flexible in single load Fe-HAO (red) than Fe/Fe-HAO (black).

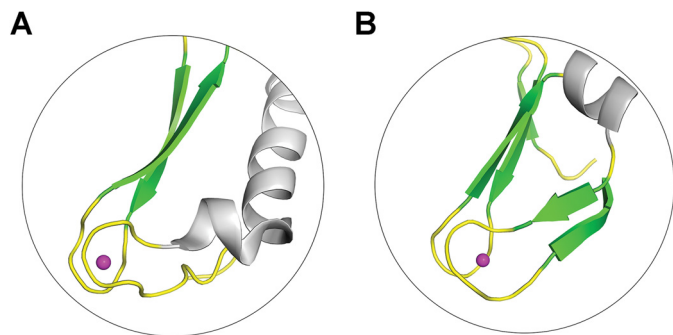


FIGURE 7. **The rubredoxin-like iron-binding site of HAO is similar to that of an iron-storage protein, Dph4.** The PDB access codes for HAO (A) and Dph4 (B) are 4L2N and 2L6L, respectively.

iron ion and it is exposed to the solvent (9). Therefore, the $[\text{Fe}(\text{Cys})_4]$ center would not need to participate in substrate binding or product release. Otherwise, HAO from all sources

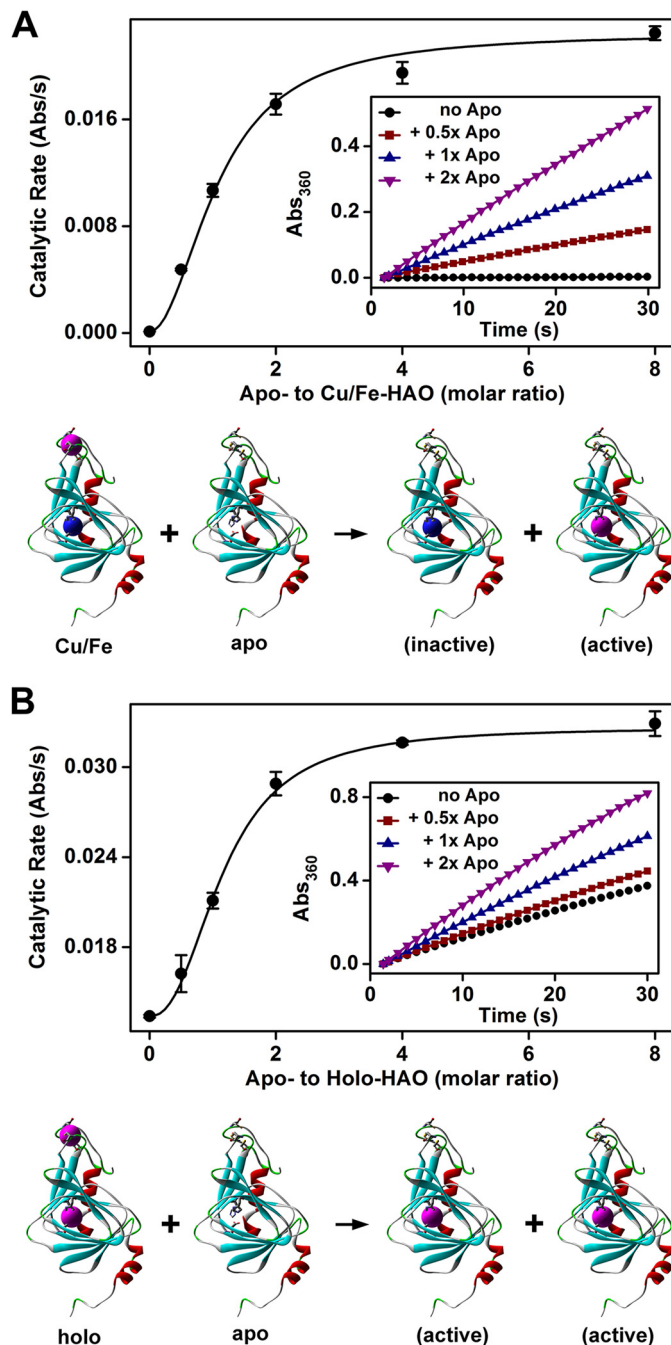


FIGURE 8. **The rubredoxin-like site of HAO replenishes iron to the catalytic site.** *A*, addition of apo-HAO (minimally active) to Cu/Fe-HAO (minimally active) produced catalytically active enzyme; *B*, addition of apo-HAO to holo-HAO doubled the total catalytic activity. Cu/Fe-HAO or holo-HAO was premixed with apo-HAO at different ratios. The catalytic activity of each sample was measured by monitoring the product formation at 360 nm at a saturating substrate concentration of $200 \mu\text{M}$ with the final concentration of Cu/Fe-HAO or holo-HAO at 10 nM . For each sample, the residual activity from apo-HAO (determined separately from control experiments) was deducted from the observed activity to determine the effective activity for comparison. The data were fitted to the Hill equation with a Hill coefficient of 2.00 and 2.36 for *A* and *B*, respectively. The insets show representative kinetic traces. For each trace, the absorbance at the starting point was subtracted to correct for background.

should have this accessory metal center for its catalytic function. Furthermore, the product channeling through the $[\text{Fe}(\text{Cys})_4]$ center, if true, would have an impact on the pathway

A Spare Tire to the Catalytic Metal

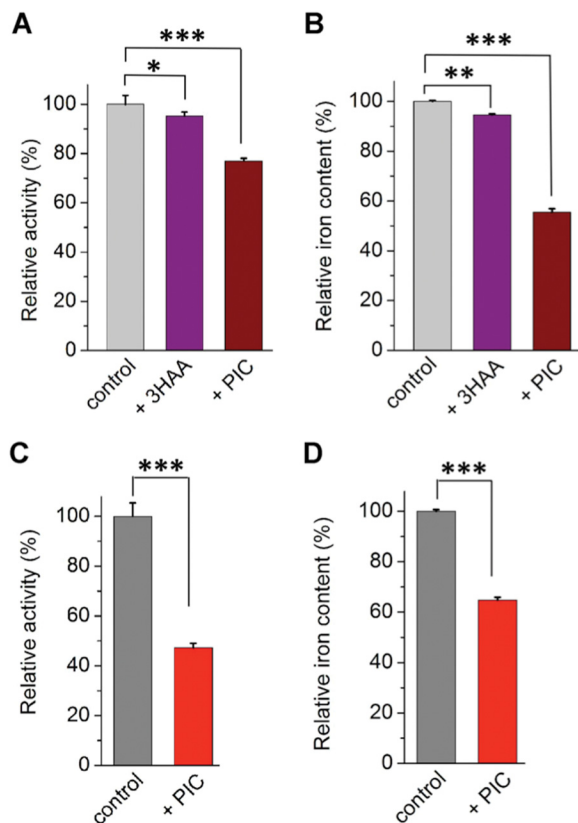


FIGURE 9. PIC removes the catalytic iron of HAO in the isolated protein and cell lysates. Isolated HAO reconstituted with 1 eq of Fe^{2+} was incubated with 3-HAA or PIC (2 mM) and analyzed by steady-state kinetic assays (A) and ICP-OES analysis (B). Exogenous 3-HAA or PIC was removed from the samples via a desalting column prior to the kinetic and spectroscopic analyses. Similarly, *E. coli* cell lysates containing overexpressed HAO were incubated with PIC (2 mM) and analyzed by steady-state kinetic assays (C) and ICP-OES analysis (D). After incubation, HAO was purified with a nickel-affinity column and desalted prior to subsequent analyses. *, $p < 0.05$; **, $p < 0.01$; and ***, $p < 0.001$.

profiling. The metabolic pathway divides immediately after the HAO-mediated chemical reaction. A decarboxylase, ACMSD (PDB entry 4OFC) (47), competes with a non-enzymatic reaction to direct the major metabolic flux to the enzyme-mediated route and allows only a minor fraction to produce quinolinic acid (Fig. 1) (19, 48). We have also considered possible product channeling between HAO and ACMSD, but our docking models of the two proteins did not yield any protein-protein interactions involving the rubredoxin-like domain (not shown). Therefore, a regulatory role of the rubredoxin center via product channeling through protein-protein interactions is unlikely.

Instead, we found that the iron ion in the rubredoxin-like domain is readily delivered to the catalytic site of the apoenzyme, *i.e.* the metal reservoir. Such an understanding has been elucidated by our spectroscopic, kinetic, structural, and metal analysis data. Our computational study shows that the iron-binding affinity at the catalytic center is higher than the non-catalytic site, with a binding energy difference of ~ 10 kcal/mol. Metal-binding dynamics will, therefore, dictate metal redistribution, due to the different metal binding affinities at the two sites. Furthermore, this calculated difference in binding affinity agrees with our kinetic, spectroscopic, and structural data to

ensure that the proposed intermolecular iron shuttling model is based upon both the experimental and theoretical evidence.

Demonstration of Iron Transfer for Catalytic Activity Restoration—Next, we show that there is indeed a need to replenish the catalytic iron during or after a highly active metabolic state, and that the iron ion will be relocated to the catalytic center. The results presented in Fig. 8 unambiguously indicates the capability of iron transfer between the two iron centers, from the rubredoxin-like site of Cu/Fe- or holo-HAO to the catalytic site of apo-HAO. It appears that the protein has tuned the iron-binding affinity of the rubredoxin-like site to an ideal point for transient iron storage in the enzyme, as a “spare tire” for the catalytic iron ion. Because the amount of iron bound to the catalytic site is the limiting factor for the observed dioxygenase activity and holo-HAO was the sole source of iron in the set of experiments shown in Fig. 8B, the theoretical maximum activity, assuming complete iron transfer from the accessory site of holo-HAO to the catalytic site of apo-HAO, is twice that of the initial activity of holo-HAO alone. Therefore, the observed doubling of activity as apo-HAO was titrated to holo-HAO supports a hypothesis that iron is transferred from the $(\text{Cys})_4$ site to the empty catalytic site of the metal-free enzyme, increasing the population of catalytically active protein molecules and leading to restoration of catalytic activity. Likewise, when Cu/Fe-HAO was the sole source of iron ions, the maximal catalytic activity obtained was close to a singly charged Fe-HAO (Fig. 8A). This observation cannot be explained by an intramolecular iron transfer model, because the Mössbauer data (Fig. 4A) and the activity assays (Fig. 3) show that iron cannot replace copper at the catalytic site.

Furthermore, the oligomerization state of HAO, which has been crystallized as a dimer (9),⁹ also points toward an intermolecular iron transfer model. In the quaternary structure, the two catalytic sites sit in the center of a heart-shaped dimer configuration, whereas the rubredoxin-like sites are positioned at the two wings, distinct from the catalytic sites. For intramolecular iron transfer to occur, the rubredoxin-like iron must traverse 24 Å to the closest catalytic site within the dimer and no apparent structural fluctuations have been observed indicating this possibility. It should be pointed out that the structural data does not provide an apparent pathway for intramolecular iron transfer, such a possibility cannot be ruled out.

Another possibility is that the iron shuttling mechanism could be linked to the iron oxidation state. However, the proteins inside the cell are in a reduced environment and the catalytically competent form of HAO is the ferrous state. Therefore, one would also anticipate that the rubredoxin-like site of HAO is in the ferrous state *in vivo*. The rubredoxin-like site in HAO has been previously suggested to be able to absorb leaking oxidative equivalents generated at the catalytic center from autooxidation of the enzyme (15). This would further indicate that the iron ion in this site is in a reduced state.

At this stage, an intermolecular iron delivery mechanism is established. However, it remains unclear if the iron ion is trans-

⁹ One monomer is present in each asymmetric unit. However, each monomer has extensive interactions with a monomer in the neighboring asymmetric unit and forms a heart-shaped dimer.

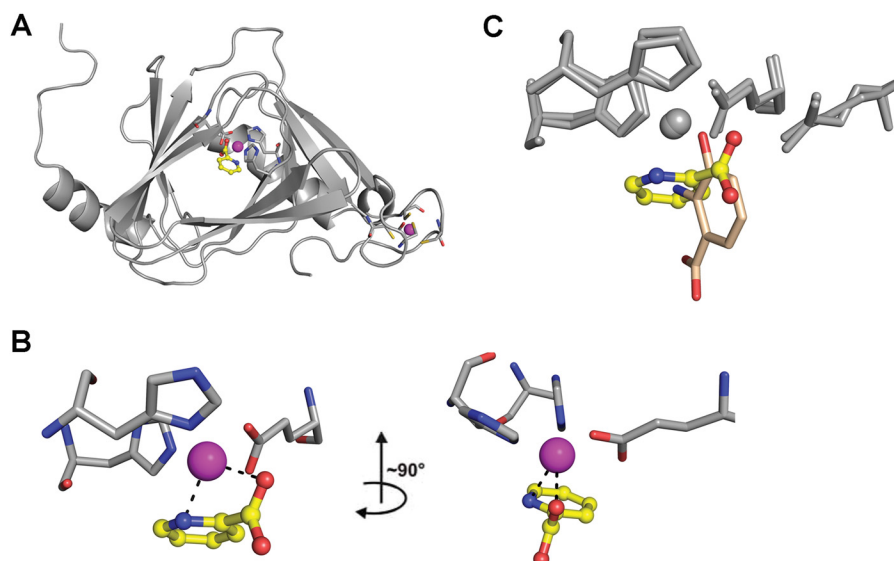


FIGURE 10. The x-ray crystal structure of HAO in complex with PIC at 1.88-Å resolution shows that PIC bidentately chelates the catalytic iron ion. A, structure of HAO with a PIC bound at the active site. PIC is shown by sticks and the metal center is represented by magenta sphere; B, PIC is bidentately bound to the iron ion in the active site. C, an overlay of the active-site structures of PIC- and 3-HAA-bound HAO.

TABLE 2
Representative functional roles of iron-bound rubredoxin-like domains

Protein name	Organism	Proposed function ^a	PDB entry	Ref.
Rubredoxin	<i>Clostridium pasteurianum</i>	Electron transfer	4RXN	53
Desulfoferrodoxin	<i>Desulfovibrio desulfuricans</i>	Electron transfer	1DFX	54
Desulfoferrodoxin	<i>Dosidicus gigas</i>	Electron transfer	1DXG	55
Rubrerythrin	<i>Desulfovibrio vulgaris</i>	Electron transfer	1RYT	56
Nigerythrin	<i>Desulfovibrio vulgaris</i>	Electron transfer	1YUX	57
DiaA	<i>Clostridium kluyver</i>	Electron transfer	N/A	58
CBS-rubredoxin-like protein (TA0289)	<i>Thermoplasma acidophilum</i>	Electron transfer	2QH1	59
High molecular weight rubredoxin (Hrb)	<i>Moorella thermoacetica</i>	Electron transfer	N/A	36
Dph4/Kti11	<i>S. cerevisiae</i>	Electron transfer	1YOP (zinc-bound)	61
Adenylate kinase	<i>Dosidicus gigas</i>	Structural	3L0P	62
Rare-cutting restriction endonuclease (NotI)	<i>Nocardia otitidiscaviarum</i>	Structural	3C25	63
Class III ribonucleotide reductase (RNR)	Enterobacteria phage T4	Structural	1H7A	5
Protein kinase G (PknG)	<i>Mycobacterium tuberculosis</i>	Structural	2PZI (cadmium-bound)	64, 65
YciM	<i>Escherichia coli</i>	Structural redox regulation	N/A	66
FdhE	<i>Pseudomonas aeruginosa</i>	Structural redox regulation	2FIY	67
Hepcidin	<i>Homo sapiens</i>	Iron-dependent regulation protein self-maturation	2KEF (apo form)	14, 18
Rubperoxin	<i>Clostridium acetobutylicum</i>	Catalysis	N/A	49
HAO	<i>Cupriavidus metallidurans</i>	Iron binding and shuttling	4L2N	This work

^a Proposed function as suggested in the references cited.

ferred through transient protein-protein interactions or free diffusion in the buffer.

Potential Physiological Relevance of the Iron-shuttling Mechanism—Rubredoxin-like $[\text{Fe}(\text{Cys})_4]$ centers are prevalent in nature. Their primary function, other than the default structural role, is typically to mediate electron transfer (1), although there are isolated reports of alternative functions such as catalysis (49) and protection from oxidative stress (50) (Table 2). The present work proposes a new function of this canonical iron center for endogenous iron binding and shuttling. The biochemical and structural results collectively suggest that the rubredoxin-like iron center of HAO plays a reservoir role, to replenish the catalytic iron if it is lost. Loss of the metal cofactor during catalysis or transient equilibrium has been previously reported in HAO (42) and in other non-enzymatic and enzymatic systems (51, 52). Here, we show that a downstream metabolic intermediate, PIC, effectively chelates and removes the catalytic iron from HAO (Figs. 9 and 10). Although our computational results indicate that the chelation of the rubredoxin-

like iron would be thermodynamically favorable, the tetrahedral coordination geometry of the rubredoxin-like iron provides steric hindrance limiting the accessibility of chelating compounds. In contrast, the active site iron has two weakly associated water ligands (Fig. 5A) that can be replaced by substrate binding (9, 15). Chelating compounds, with a structure similar to that of the substrate, would take advantage of these transient coordination sites to potentially chelate and remove the catalytic metal.

In the kynurenine pathway, PIC is the downstream metabolic dead-end product of the nonenzymatic cyclization of 2-aminomuconate-6-semialdehyde, the product of ACMSD (Fig. 1). During high metabolic activity, the utilization of a nonenzymatically produced metabolic dead-end to regulate an upstream enzyme, allows for a continuous metabolic flux through the pathway while temporarily slowing it down to prevent the further accumulation of PIC. This feedback inhibition mechanism and our newly discovered iron-shuttling mechanism, which restores catalytic activity, provide a pos-

A Spare Tire to the Catalytic Metal

sible explanation of the chemical control over the kynurenine pathway.

HAO in multicellular organisms is solely involved in tryptophan catabolism, which is not a primary energy source. However, in single-cell organisms, the carbon, nitrogen, and energy sources are often derived from the degradation of a single organic compound either naturally or through directed evolution. HAO breaks the aromaticity of the phenyl ring, chemically the most difficult step in these pathways, and hence it is critical for life-sustaining processes in these lower organisms. Thus, the replenishment of the catalytic iron by the accessory metal center becomes essential to the survival of these organisms but not in multicellular organisms.

The rubredoxin-like motif is ubiquitous in nature, yet very little is known regarding its biological functions. Other than the default structural role, it is often proposed to participate in electron transfer. For the first time we show that a rubredoxin-like iron-sulfur center in an iron-dependent dioxygenase is capable of functioning as a “spare tire” for replenishing the catalytic iron if it becomes stripped by a pool of metal-chelating metabolic intermediates. This idea will be further tested in future biochemical and cellular studies in many of the enzymes and proteins that contain an accessory rubredoxin-like domain. Hence, the results presented are significant for expanding our understanding of such prevalent iron-sulfur centers in biological systems.

Acknowledgments—Mössbauer spectroscopy data were collected at the National High Magnetic Field Laboratory, which is funded by the NSF through the Cooperative Agreement No. DMR-1157490, the State of Florida, and the DOE. The Mössbauer spectrometer was funded by the User Collaboration Grants Program Award 5064 (2007) (to A. O.). X-ray diffraction data were collected at the Southeast Regional Collaborative Access Team (SER-CAT) 22-ID beamline with the Advanced Photon Source at the Argonne National Laboratory. The use of the Advanced Photon Source was supported by DOE, Office of Science, Office of Basic Energy Sciences, under Contract W-31-109-Eng-38.

References

- Orme-Johnson, W. H. (1973) Iron-sulfur proteins: structure and function. *Annu. Rev. Biochem.* **42**, 159–204
- Lovenberg, W., and Sobel, B. E. (1965) Rubredoxin: a new electron transfer protein from *Clostridium pasteurianum*. *Proc. Natl. Acad. Sci. U.S.A.* **54**, 193–199
- Adam, V., Royant, A., Nivière, V., Molina-Heredia, F. P., and Bourgeois, D. (2004) Structure of superoxide reductase bound to ferrocyanide and active site expansion upon x-ray-induced photo-reduction. *Structure* **12**, 1729–1740
- Logan, D. T., Mulliez, E., Larsson, K. M., Bodevin, S., Atta, M., Garnaud, P. E., Sjöberg, B. M., and Fontecave, M. (2003) A metal-binding site in the catalytic subunit of anaerobic ribonucleotide reductase. *Proc. Natl. Acad. Sci. U.S.A.* **100**, 3826–3831
- Larsson, K. M., Andersson, J., Sjöberg, B. M., Nordlund, P., and Logan, D. T. (2001) Structural basis for allosteric substrate specificity regulation in anaerobic ribonucleotide reductases. *Structure* **9**, 739–750
- Ichiyama, A., Nakamura, S., Kawai, H., Honjo, T., Nishizuka, Y., Hayaishi, O., and Senoh, S. (1965) Studies on the metabolism of the benzene ring of tryptophan in mammalian tissues: II. enzymatic formation of α -amino-muconic acid from 3-hydroxyanthranilic acid. *J. Biol. Chem.* **240**, 740–749
- Muraki, T., Taki, M., Hasegawa, Y., Iwaki, H., and Lau, P. C. (2003) Prokaryotic homologs of the eukaryotic 3-hydroxyanthranilate 3,4-dioxygenase and 2-amino-3-carboxymuconate-6-semialdehyde decarboxylase in the 2-nitrobenzoate degradation pathway of *Pseudomonas fluorescens* strain KU-7. *Appl. Environ. Microbiol.* **69**, 1564–1572
- Kurnasov, O., Goral, V., Colabroy, K., Gerdes, S., Anantha, S., Osterman, A., and Begley, T. P. (2003) NAD biosynthesis: identification of the tryptophan to quinolinate pathway in bacteria. *Chem. Biol.* **10**, 1195–1204
- Zhang, Y., Colabroy, K. L., Begley, T. P., and Ealick, S. E. (2005) Structural studies on 3-hydroxyanthranilate-3,4-dioxygenase: the catalytic mechanism of a complex oxidation involved in NAD biosynthesis. *Biochemistry* **44**, 7632–7643
- Dunwell, J. M., Culham, A., Carter, C. E., Sosa-Aguirre, C. R., and Goodenough, P. W. (2001) Evolution of functional diversity in the cupin superfamily. *Trends Biochem. Sci.* **26**, 740–746
- Hegg, E. L., and Que, L., Jr. (1997) The 2-His-1-carboxylate facial triad: an emerging structural motif in mononuclear non-heme iron(II) enzymes. *Eur. J. Biochem.* **250**, 625–629
- Li, X., Guo, M., Fan, J., Tang, W., Wang, D., Ge, H., Rong, H., Teng, M., Niu, L., Liu, Q., and Hao, Q. (2006) Crystal structure of 3-hydroxyanthranilic acid 3,4-dioxygenase from *Saccharomyces cerevisiae*: a special subgroup of the type III extradiol dioxygenases. *Protein Sci.* **15**, 761–773
- Dilović, I., Glubič, F., Malpeli, G., Zanotti, G., and Matković-Calogović, D. (2009) Crystal structure of bovine 3-hydroxyanthranilate 3,4-dioxygenase. *Biopolymers* **91**, 1189–1195
- Jordan, J. B., Poppe, L., Haniu, M., Arvedson, T., Syed, R., Li, V., Kohno, H., Kim, H., Schnier, P. D., Harvey, T. S., Miranda, L. P., Cheetham, J., and Sasu, B. J. (2009) Hepcidin revisited, disulfide connectivity, dynamics, and structure. *J. Biol. Chem.* **284**, 24155–24167
- Colabroy, K. L., Zhai, H., Li, T., Ge, Y., Zhang, Y., Liu, A., Ealick, S. E., McLafferty, F. W., and Begley, T. P. (2005) The mechanism of inactivation of 3-hydroxyanthranilate-3,4-dioxygenase by 4-chloro-3-hydroxyanthranilate. *Biochemistry* **44**, 7623–7631
- Jones, D. T., Taylor, W. R., and Thornton, J. M. (1992) The rapid generation of mutation data matrices from protein sequences. *Comput. Appl. Biosci.* **8**, 275–282
- Tamura, K., Stecher, G., Peterson, D., Filipinski, A., and Kumar, S. (2013) MEGA6: Molecular Evolutionary Genetics Analysis version 6.0. *Mol. Biol. Evol.* **30**, 2725–2729
- Farnaud, S., Rapisarda, C., Bui, T., Drake, A., Cammack, R., and Evans, R. W. (2008) Identification of an iron-hepcidin complex. *Biochem. J.* **413**, 553–557
- Li, T., Walker, A. L., Iwaki, H., Hasegawa, Y., and Liu, A. (2005) Kinetic and spectroscopic characterization of ACMSD from *Pseudomonas fluorescens* reveals a pentacoordinate mononuclear metallocofactor. *J. Am. Chem. Soc.* **127**, 12282–12290
- Li, T., Iwaki, H., Fu, R., Hasegawa, Y., Zhang, H., and Liu, A. (2006) α -Amino- β -carboxymuconate- ϵ -semialdehyde decarboxylase (ACMSD) is a new member of the amidohydrolase superfamily. *Biochemistry* **45**, 6628–6634
- Huo, L., Davis, I., Chen, L., and Liu, A. (2013) The power of two: arginine 51 and arginine 239* from a neighboring subunit are essential for catalysis in α -amino- β -carboxymuconate- ϵ -semialdehyde decarboxylase. *J. Biol. Chem.* **288**, 30862–30871
- Ozarowski, A., Lee, H. M., and Balch, A. L. (2003) Crystal environments probed by EPR spectroscopy. Variations in the EPR spectra of Co-II(octaethylporphyrin) doped in crystalline diamagnetic hosts and a reassessment of the electronic structure of four-coordinate cobalt(II). *J. Am. Chem. Soc.* **125**, 12606–12614
- Vagin, A., and Teplyakov, A. (2010) Molecular replacement with MOLREP. *Acta Crystallogr. D Biol. Crystallogr.* **66**, 22–25
- Emsley, P., and Cowtan, K. (2004) Coot: model-building tools for molecular graphics. *Acta Crystallogr. D Biol. Crystallogr.* **60**, 2126–2132
- Andrejasic, M., Praaenikar, J., and Turk, D. (2008) PURY: a database of geometric restraints of hetero compounds for refinement in complexes with macromolecular structures. *Acta Crystallogr. D Biol. Crystallogr.* **64**, 1093–1109
- Hornak, V., Abel, R., Okur, A., Strockbine, B., Roitberg, A., and Simmer-

- ling, C. (2006) Comparison of multiple Amber force fields and development of improved protein backbone parameters. *Proteins* **65**, 712–725
27. Case, D. A., Cheatham, T. E., 3rd, Darden, T. A., Gohlke, H., Luo, R., Merz, K. M., Jr., Onufriev, A., Simmerling, C., Wang, B., and Woods, R. J. (2005) The Amber biomolecular simulation programs. *J. Comput. Chem.* **26**, 1668–1688
 28. Jorgensen, W. L. (1982) Revised TIPS for simulations of liquid water and aqueous solutions. *J. Chem. Phys.* **77**, 4156–4163
 29. Ryckaert, J.-P., Ciccotti, G., and Berendsen, H. J. C. (1977) Numerical integration of the cartesian equations of motion of a system with constraints: molecular dynamics of *n*-alkanes. *J. Comp. Chem.* **23**, 327–341
 30. Larini, L., Mannella, R., and Leporini, D. (2007) Langevin stabilization of molecular-dynamics simulations of polymers by means of quasisymplectic algorithms. *J. Chem. Phys.* **126**, 104101
 31. Cerutti, D. S., Duke, R. E., Darden, T. A., and Lybrand, T. P. (2009) Staggered mesh Ewald: an extension of the smooth particle-mesh Ewald method adding great versatility. *J. Chem. Theory Comput.* **5**, 2322
 32. Anandkrishnan, R., Aguilar, B., and Onufriev, A. V. (2012) H++ 3.0: automating pK prediction and the preparation of biomolecular structures for atomistic molecular modeling and simulations. *Nucleic Acids Res.* **40**, W537–W541
 33. Hausinger, R. P. (2004) Fe(II)/ α -ketoglutarate-dependent hydroxylases and related enzymes. *Crit. Rev. Biochem. Mol. Biol.* **39**, 21–68
 34. van der Donk, W. A., Krebs, C., and Bollinger, J. M., Jr. (2010) Substrate activation by iron superoxo intermediates. *Curr. Opin. Struct. Biol.* **20**, 673–683
 35. Arciero, D. M., Lipscomb, J. D., Huynh, B. H., Kent, T. A., and Münck, E. (1983) EPR and Mössbauer studies of protocatechuate 4,5-dioxygenase: characterization of a new Fe²⁺ environment. *J. Biol. Chem.* **258**, 14981–14991
 36. Silaghi-Dumitrescu, R., Coulter, E. D., Das, A., Ljungdahl, L. G., Jameson, G. N., Huynh, B. H., and Kurtz, D. M., Jr. (2003) A flavodiiron protein and high molecular weight rubredoxin from *Moorella thermoacetica* with nitric oxide reductase activity. *Biochemistry* **42**, 2806–2815
 37. Moura, I., Tavares, P., Moura, J. J., Ravi, N., Huynh, B. H., Liu, M. Y., and LeGall, J. (1990) Purification and characterization of desulfoferrodoxin: a novel protein from *Desulfovibrio desulfuricans* (ATCC 27774) and from *Desulfovibrio vulgaris* (strain Hildenborough) that contains a distorted rubredoxin center and a mononuclear ferrous center. *J. Biol. Chem.* **265**, 21596–21602
 38. Thakur, A., Chitoor, B., Goswami, A. V., Pareek, G., Atreya, H. S., and D'Silva, P. (2012) Structure and mechanistic insights into novel iron-mediated moonlighting functions of human J-protein cochaperone, Dph4. *J. Biol. Chem.* **287**, 13194–13205
 39. Minakata, K., Fukushima, K., Nakamura, M., and Iwahashi, H. (2011) Effect of some naturally occurring iron ion chelators on the formation of radicals in the reaction mixtures of rat liver microsomes with ADP, Fe³⁺ and NADPH. *J. Clin. Biochem. Nutr.* **49**, 207–215
 40. Evans, G. W. (1982) The role of picolinic acid in metal metabolism. *Life Chem. Rep.* **1**, 57–67
 41. Mikogami, T., Marianne, T., and Spik, G. (1995) Effect of intracellular iron depletion by picolinic acid on expression of the lactoferrin receptor in the human colon carcinoma cell subclone HT29–18-C1. *Biochem. J.* **308**, 391–397
 42. Koontz, W. A., and Shiman, R. (1976) Beef kidney 3-hydroxyanthranilic acid oxygenase. Purification, characterization, and analysis of the assay. *J. Biol. Chem.* **251**, 368–377
 43. Lesuisse, E., Simon, M., Klein, R., and Labbe, P. (1992) Excretion of anthranilate and 3-hydroxyanthranilate by *Saccharomyces cerevisiae*: relationship to iron-metabolism. *J. Gen. Microbiol.* **138**, 85–89
 44. Kim, C., Lorenz, W. W., Hoopes, J. T., and Dean, J. F. (2001) Oxidation of phenolate siderophores by the multicopper oxidase encoded by the *Escherichia coli* yacK gene. *J. Bacteriol.* **183**, 4866–4875
 45. Ogasawara, N., Gander, J. E., and Henderson, L. M. (1966) Purification and properties of 3-hydroxyanthranilate oxygenase from beef kidney. *J. Biol. Chem.* **241**, 613–619
 46. Franco, R., Moura, J. J. G., and Ferreira, G. C. (1999) *Iron metabolism: inorganic biochemistry and regulatory mechanisms*, pp. 341–355, Wiley-VCH, New York
 47. Huo, L., Liu, F., Iwaki, H., Li, T., Hasegawa, Y., and Liu, A. (2015) Human α -amino- β -carboxymuconate- ϵ -semialdehyde decarboxylase (ACMSD): a structural and mechanistic unveiling. *Proteins* **83**, 178–187
 48. Li, T., Walker, A. L., Iwaki, H., Hasegawa, Y., and Liu, A. (2007) Detection of transient intermediates in the metal-dependent nonoxidative decarboxylation catalyzed by α -amino- β -carboxymuconate- ϵ -semialdehyde. *J. Am. Chem. Soc.* **129**, 9278–9279
 49. Kawasaki, S., Ono, M., Watamura, Y., Sakai, Y., Satoh, T., Arai, T., Satoh, J., and Niimura, Y. (2007) An O₂-inducible rubrerythrin-like protein, rubperoxin, is functional as a H₂O₂ reductase in an obligatory anaerobe *Clostridium acetobutylicum*. *FEBS Lett.* **581**, 2460–2464
 50. Coulter, E. D., and Kurtz, D. M., Jr. (2001) A role for rubredoxin in oxidative stress protection in *Desulfovibrio vulgaris*: catalytic electron transfer to rubrerythrin and two-iron superoxide reductase. *Arch. Biochem. Biophys.* **394**, 76–86
 51. Sheldon, R. A., Wallau, M., Arends, I. W. C. E., and Schuchardt, U. (1998) Heterogeneous catalysts for liquid-phase oxidations: philosophers' stones or Trojan horses? *Acc. Chem. Res.* **31**, 485–493
 52. Varghese, S., Tang, Y., and Imlay, J. A. (2003) Contrasting sensitivities of *Escherichia coli* aconitases A and B to oxidation and iron depletion. *J. Bacteriol.* **185**, 221–230
 53. Watenpaugh, K. D., Sieker, L. C., and Jensen, L. H. (1980) Crystallographic refinement of rubredoxin at 1.2 Å resolution. *J. Mol. Biol.* **138**, 615–633
 54. Coelho, A. V., Matias, P., Fulop, V., Thompson, A., Gonzalez, A., and Carrondo, M. A. (1997) Desulfoferrodoxin structure determined by MAD phasing and refinement to 1.9 Å resolution reveals a unique combination of a tetrahedral FeS₄ centre with a square pyramidal FeSN₄ centre. *J. Biol. Inorg. Chem.* **2**, 680–689
 55. Archer, M., Huber, R., Tavares, P., Moura, I., Moura, J. J., Carrondo, M. A., Sieker, L. C., LeGall, J., and Romão, M. J. (1995) Crystal structure of desulfoferrodoxin from *Desulfovibrio gigas* determined at 1.8 Å resolution: a novel non-heme iron protein structure. *J. Mol. Biol.* **251**, 690–702
 56. Jin, S., Kurtz, D. M., Jr., Liu, Z. J., Rose, J., and Wang, B. C. (2002) X-ray crystal structures of reduced rubrerythrin and its azide adduct: a structure-based mechanism for a non-heme diiron peroxidase. *J. Am. Chem. Soc.* **124**, 9845–9855
 57. Iyer, R. B., Silaghi-Dumitrescu, R., Kurtz, D. M., Jr., and Lanzilotta, W. N. (2005) High-resolution crystal structures of *Desulfovibrio vulgaris* (Hildenborough) nigerythrin: facile, redox-dependent iron movement, domain interface variability, and peroxidase activity in the rubrerythrins. *J. Biol. Inorg. Chem.* **10**, 407–416
 58. Chakraborty, S., Sakka, M., Kimura, T., and Sakka, K. (2008) Cloning and expression of a *Clostridium kluyveri* gene responsible for diaphorase activity. *Biosci. Biotechnol. Biochem.* **72**, 735–741
 59. Proudfoot, M., Sanders, S. A., Singer, A., Zhang, R., Brown, G., Binkowski, A., Xu, L., Lukin, J. A., Murzin, A. G., Joachimiak, A., Arrowsmith, C. H., Edwards, A. M., Savchenko, A. V., and Yakunin, A. F. (2008) Biochemical and structural characterization of a novel family of cystathionine β -synthase domain proteins fused to a Zn ribbon-like domain. *J. Mol. Biol.* **375**, 301–315
 60. Sun, J., Zhang, J., Wu, F., Xu, C., Li, S., Zhao, W., Wu, Z., Wu, J., Zhou, C. Z., and Shi, Y. (2005) Solution structure of Kti11p from *Saccharomyces cerevisiae* reveals a novel zinc-binding module. *Biochemistry* **44**, 8801–8809
 61. Dong, M., Su, X., Dzikovski, B., Dando, E. E., Zhu, X., Du, J., Freed, J. H., and Lin, H. (2014) Dph3 is an electron donor for Dph1–Dph2 in the first step of eukaryotic diphthamide biosynthesis. *J. Am. Chem. Soc.* **136**, 1754–1757
 62. Mukhopadhyay, A., Kladova, A. V., Bursakov, S. A., Gavel, O. Y., Calvete, J. J., Shnyrov, V. L., Moura, I., Moura, J. J., Romão, M. J., and Trincão, J. (2011) Crystal structure of the zinc-, cobalt-, and iron-containing adenylate kinase from *Desulfovibrio gigas*: a novel metal-containing adenylate kinase from Gram-negative bacteria. *J. Biol. Inorg. Chem.* **16**, 51–61
 63. Lambert, A. R., Sussman, D., Shen, B., Maunus, R., Nix, J., Samuelson, J., Xu, S. Y., and Stoddard, B. L. (2008) Structures of the rare-cutting restriction endonuclease NotI reveal a unique metal binding fold involved in

A Spare Tire to the Catalytic Metal

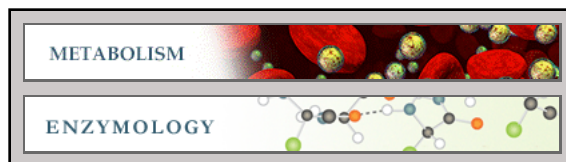
- DNA binding. *Structure* **16**, 558–569
64. Gil, M., Graña, M., Schopfer, F. J., Wagner, T., Denicola, A., Freeman, B. A., Alzari, P. M., Batthyány, C., and Durán, R. (2013) Inhibition of *Mycobacterium tuberculosis* PknG by non-catalytic rubredoxin domain specific modification: reaction of an electrophilic nitro-fatty acid with the Fe-S center. *Free Radic. Biol. Med.* **65**, 150–161
65. Scherr, N., Honnappa, S., Kunz, G., Mueller, P., Jayachandran, R., Winkler, F., Pieters, J., and Steinmetz, M. O. (2007) Structural basis for the specific inhibition of protein kinase G, a virulence factor of *Mycobacterium tuberculosis*. *Proc. Natl. Acad. Sci. U.S.A.* **104**, 12151–12156
66. Nicolaes, V., El Hajjaji, H., Davis, R. M., Van der Henst, C., Depuydt, M., Leverrier, P., Aertsen, A., Haufroid, V., Ollagnier de Choudens, S., De Bolle, X., Ruiz, N., and Collet, J. F. (2014) Insights into the function of YciM, a heat-shock membrane protein required to maintain envelope integrity in *Escherichia coli*. *J. Bacteriol.* **196**, 300–309
67. Lüke, I., Butland, G., Moore, K., Buchanan, G., Lyall, V., Fairhurst, S. A., Greenblatt, J. F., Emili, A., Palmer, T., and Sargent, F. (2008) Biosynthesis of the respiratory formate dehydrogenases from *Escherichia coli*: characterization of the FdhE protein. *Arch. Microbiol.* **190**, 685–696

Metabolism:

**An Iron Reservoir to the Catalytic Metal:
THE RUBREDOXIN IRON IN AN
EXTRADIOL DIOXYGENASE**

Fange Liu, Jiafeng Geng, Ryan H. Gumpper,
Arghya Barman, Ian Davis, Andrew
Ozarowski, Donald Hamelberg and Aimin Liu
J. Biol. Chem. 2015, 290:15621-15634.

doi: 10.1074/jbc.M115.650259 originally published online April 27, 2015



Access the most updated version of this article at doi: [10.1074/jbc.M115.650259](https://doi.org/10.1074/jbc.M115.650259)

Find articles, minireviews, Reflections and Classics on similar topics on the [JBC Affinity Sites](http://www.jbc.org/).

Alerts:

- [When this article is cited](#)
- [When a correction for this article is posted](#)

[Click here](#) to choose from all of JBC's e-mail alerts

This article cites 66 references, 21 of which can be accessed free at
<http://www.jbc.org/content/290/25/15621.full.html#ref-list-1>